Check for updates

ChemElectroChem

Research Article
doi.org/10.1002/celc.202400563

Chemistry Europe
European Chemical Societies Publishing

www.chemelectrochem.org

A Comparative Study of the Oxygen Reduction Reaction on Pt and Ag in Alkaline Media

Alexander Rampf,[a] Michael Braig,[a] Stefano Passerini,[a, b] and Roswitha Zeis*[a, c, d]

Investigating the ORR under practical conditions is vital for optimizing metal–air batteries and alkaline fuel cells. Herein, we characterized Pt and Ag gas diffusion electrodes (GDE) in a GDE half-cell in high alkaline concentrations at elevated temperatures by polarization curves and electrochemical impedance spectroscopy (EIS) combined with the distribution of relaxation times (DRT) analysis. The Pt catalyst's polarization curve displays substantial losses below 0.82 V vs. RHE. The DRT analysis reveals significantly increased charge transfer resistance and a decelerated ORR at that potential. RRDE measurements attributed the polarization loss observed for Pt catalysts to increased peroxide formation in this potential region triggered by the desorption of oxygenated species. Therefore, the ORR activity of Ag exceeds some of the here-used Pt catalysts at high current densities. This work combines the benefits of the RRDE and the GDE half-cell to study catalysts and identify the reaction mechanisms under conditions relevant to practical fuel cells and batteries. Moreover, the DRT analysis is introduced as an analytical tool to determine the charge transfer resistance contribution and the corresponding frequency of the ORR.

1. Introduction

The Oxygen Reduction Reaction (ORR) is one of the most widely studied topics in catalysis and electrochemistry because it plays a fundamental role in energy storage and conversion devices such as fuel cells and metal–air batteries.[1] The ORR process requires many individual steps and a major molecular reorganization. This reaction is, therefore, the kinetically limiting factor of these technical devices. In the last decades, intensive research has been undertaken to understand the ORR mechanism and to find highly active catalysts to reduce the overpotential. For maximum activity, a balance between the kinetics of the O–O bond cleavage, the electroreduction of the oxygenated intermediates, and the O–H formation should be achieved.[2] Platinum (Pt) is regarded as the best single-metal catalyst for the ORR.[1] However, Pt's drawbacks are its scarcity in the earth's crust, non-sustainable mining, and high costs.[3–5] Unlike in acidic electrolytes, the ORR in alkaline media offers the possibility of using other types of catalysts besides Pt since these catalysts are stable in alkaline and achieve substantial ORR activities. Silver (Ag) can be employed as an alternative catalyst material with relatively low cost (ca. 1% of Pt) and high activity towards the ORR.[6,7] Furthermore, only small amounts of peroxide are formed over a wide pH range.[8] It is even reported that Ag exhibits a similar or more prominent catalytic activity than Pt under certain conditions.[9,10]

The ORR mechanism is not fully elucidated yet due to many involved oxygen-containing species (O, OH, O_2^-, HO_2^-, and H_2O_2), but two main pathways are identified in general.[1,11] The reaction can occur via the desired direct four-electron or the two-electron pathway. In the case of the two-electron pathway, a thermodynamically unstable peroxide ion is formed, which is very reactive and corrosive and should, therefore, be prevented.[12,13] This species can be further reduced, and this sequence is then called the $2e^- + 2e^-$ pathway. A distinction to the direct four-electron pathway is challenging because the final product is identical. Moreover, it is unclear if the direct four-electron pathway exists since it could also be a very fast $2e^- + 2e^-$ process.[1,14]

This work used the Rotating Ring-Disk Electrode (RRDE), a modified Rotating Disk Electrode (RDE) setup with an additional ring electrode, to monitor the reaction pathway on Pt and Ag at several KOH concentrations. RDE and RRDE are the methods for rapid screening of ORR catalyst activities.[15] Although these techniques are excellent for determining the catalytic activity of electrocatalysts, they do not fully reflect the conditions in the application. A half-cell with an integrated gas diffusion electrode (GDE) enables measurements under technical conditions such as high current densities (Figure S1). The technique additionally allows for the fast screening of GDEs. The time-consuming membrane electrode assembly (MEA) fabrication process can be eliminated for preliminary testing. Several ORR studies with GDE half-cells have recently been reported, whereby almost all are carried out in an acidic electrolyte.[16–23] Fewer results can be found for alkaline conditions.[24–27] This work

[a] A. Rampf, M. Braig, S. Passerini, R. Zeis
Helmholtz Institute Ulm, Karlsruhe Institute of Technology, Helmholtzstraße 11, 89081 Ulm, Germany

[b] S. Passerini
Sapienza University of Rome, Piazzale Aldo Moro 5, 00185 Roma, Italy

[c] R. Zeis
Department of Electrical Engineering, Friedrich-Alexander-Universität Erlangen-Nürnberg, Cauerstraße 9, 91058 Erlangen, Germany
E-mail: roswitha.zeis@fau.de

[d] R. Zeis
Department of Mechanical and Industrial Engineering, University of Toronto, 5 King's College Road, Toronto, Ontario M5S 3G8, Canada

Supporting information for this article is available on the WWW under https://doi.org/10.1002/celc.202400563

© 2024 The Authors. ChemElectroChem published by Wiley-VCH GmbH. This is an open access article under the terms of the Creative Commons Attribution License, which permits use, distribution and reproduction in any medium, provided the original work is properly cited.

© 2024 The Authors. ChemElectroChem published by Wiley-VCH GmbH

demonstrates, as one of the first, GDE half-cell measurements with Pt/C in a highly concentrated alkaline electrolyte, adopting the best practice recommendations for an acidic electrolyte.[16]

This study uses both techniques to analyze the ORR on Pt and Ag in detail, as shown in Table 1. It investigates the ORR performance of technical GDEs and determines reaction paths using RRDE. We demonstrate higher ORR performance for Ag than for some Pt catalysts in alkaline media under technically relevant conditions. Furthermore, the underlying processes leading to this result are identified.

Experimental Section

Reactants and Instrumentations

All chemicals used in this work were used as received without further purification. Ultrapure water (0.055 µS) from the water dispenser PURELAB®flex (Elga) was used for the syntheses, preparing the KOH solutions, and cleaning. Thermogravimetric analyses (Discovery DSC, TA instruments) were performed to determine the silver content of the synthesized Ag/C catalysts. The protocol consisted of a 10 K/min heating ramp at a pure oxygen atmosphere from 40–1000 °C. The Pt/C and Ag/C catalysts were characterized by XRD (D8 Advance, Bruker with Cu Kα radiation). The SEM images were taken with an LEO 1550 VP instrument (Carl Zeiss AG) with an acceleration voltage of 3 kV.

Synthesis of Catalysts

The synthesis of Ag/C catalysts was carried out according to a synthesis route published by Garcia et al.[28] XC 72R Vulcan carbon powder (FuelCellStore) was dispersed in water and sonicated for one hour. Afterward, $AgNO_3$ (> 99.9 %, Alfa Aesar) was added to the suspension under continuous stirring. Then, another aqueous solution containing glycerol (Rotipuran®, ≥ 99.5 %, Carl Roth) and NaOH (GPR Rectapur®, VWR) was added. The resultant concentrations achieved were 0.82 mM $AgNO_3$, 1 M glycerol, and 0.1 M NaOH. The suspension was stirred for 24 hours at room temperature. After that, it was filtered, and the remaining product was washed and dried at 80 °C for around 12 hours. The obtained powder was ground. Ag/C catalysts with 22 % and 68 % Ag content were synthesized.

Electrochemical Measurements

For the electrochemical measurements, KOH (Emplura®, Merck) electrolyte was used. All potentials in this work are given against the reversible hydrogen electrode (RHE).

RRDE Measurements

First, the RRDE electrode was polished with alumina slurry (0.05 µm, Buehler) on various Buehler polishing pads to achieve a mirror-smooth surface. Afterward, the electrode was thoroughly washed with ultrapure water and then sonicated in ultrapure water for at least five minutes. The procedure was performed before each measurement except for the silver-coated glassy carbon disk to prevent the removal of the silver coating.

For the RRDE measurements, a Research MSR Rotator (Pine Research Instrumentation) was used. They were performed at room temperature with an SP-300 potentiostat (BioLogic Science Instruments). The four-electrode setup consists of the Pine E6-series ring-disk electrode as the two working electrodes (WE). The disk and ring electrode have an area of 0.196 cm^2 and 0.110 cm^2, respectively. Gold was used as ring material since it is proven well-suited for detecting peroxides in alkaline media.[29] The disk electrode consists either of polycrystalline platinum or a silver film (100 nm) sputtered on a glassy carbon disk (GC) electrode. The sputter coater EM ACE600 (Leica Microsystems) with a silver sputtering target (99.99 %, Nanografi Nano Technology) created an ultrapure silver film. In the following, the modified electrode is called an Ag disk electrode for simplicity reasons. An in-house developed dynamic hydrogen electrode (DHE) was the reference electrode (RE). As a counter electrode (CE), a piece of thermally activated carbon felt (SIGRACELL®GFA 6.0 EA, SGL Carbon) was employed.

Before each measurement, the electrolyte was purged with nitrogen for at least 15 minutes using a PTFE gas frit (pore size: 5 µm, Bohlender). The microporous gas frit produces a sparkling gas flow, which secures a good gas distribution and a fast electrolyte saturation with the respective gas. Additionally, the electrodes were pretreated to activate the catalyst.[30,31] For polycrystalline Pt, 20 CV scans between 0.1 and 1.1 V were conducted at 50 $mV s^{-1}$ in a nitrogen-saturated electrolyte to achieve steady-state voltammograms. For Ag, the potential range was set to 0.0–1.0 V to prevent metal oxidation and dissolution.[32,33] Before the ORR measurements, oxygen was purged into the electrolyte for at least 15 minutes. Subsequently, several CVs were performed at a scan rate of 50 $mV s^{-1}$ at 100, 400, 900, 1600, and 2500 rpm rotation rates. During the measurements, the potential of the ring electrode was set to 1.3 V to detect the peroxide species formed during the ORR. Detailed information about the measurement procedure is given in Table S1.

All RRDE measurements shown in this work have been corrected in the background. To reduce the noise, the background-corrected ring currents were smoothed with the Savitzky-Golay filter with 50 points in the Origin program. This digital filter allows the smoothing of the data without distorting the signal tendency and is based on the linear least square method.[34]

A standard measurement was performed to determine the empirical collection efficiency of the RRDE.[30,35] For this, CVs were

Table 1. Summary of the pros and cons of the RDE/RRDE setup, GDE half-cell, and full cell for investigating the ORR.

RDE/RRDE	GDE Half-Cell	Full Cell
⊕ Screening of catalysts	⊕ Testing of realistic electrodes (e.g. GDEs)	⊕ Testing of technical cells
⊕ Little material consumption	⊕ Technical conditions	⊖ Long measurement times
⊕ Detection of reaction path (RRDE)	⊕ Focus on a half-cell reaction (e.g. ORR)	⊖ Large material consumption
⊖ Model cell	⊖ Moderate material consumption	

© 2024 The Authors. ChemElectroChem published by Wiley-VCH GmbH

21960216, 0, Downloaded from https://chemistry-europe.onlinelibrary.wiley.com/doi/10.1002/celc.202400563 by Karlsruher Institut F., Wiley Online Library on [23/01/2025]. See the Terms and Conditions (https://onlinelibrary.wiley.com/terms-and-conditions) on Wiley Online Library for rules of use; OA articles are governed by the applicable Creative Commons License

conducted at the Pt disk electrode at 10 mV s^{-1} from 0.0 to 1.3 V in an aqueous 0.1 M KOH electrolyte with 10 mM potassium ferricyanide $K_3Fe(CN)_6$ (AnalaR Normapur®, VWR). The Au ring electrode was kept at 1.55 V (see Figure S2). The empirical collection efficiency N_C was calculated by Equation (1).

$$N_C = -\frac{I_{ring,limiting}}{I_{disk,limiting}} \cdot 100\% \quad (1)$$

The values for the limiting currents for the disk $I_{disk,limiting}$, and for the ring electrode $I_{ring,limiting}$ were recorded in the potential range of 0.1–0.8 V. The collection efficiencies at specific rotation rates are noted in Table S2. The average collection efficiency over all measured rotation rates is (24.9 ± 0.2)%, close to the theoretical collection efficiency of 25.6% given by the manufacturer. The empirical collection efficiency N_C was used together with the disk and ring current density, j_D and j_R, to calculate the number of transferred electrons n and the percentage $X_{H_2O_2}$ of hydrogen peroxide formed during the ORR (see Equations (2) and (3)).

$$n = \frac{4j_D}{j_D + \frac{j_R}{N_C}} \quad (2)$$

$$X_{H_2O_2} = \frac{2\frac{j_R}{N_C}}{j_D + \frac{j_R}{N_C}} \cdot 100\,\% \quad (3)$$

GDE Half-Cell Measurements

Different gas diffusion electrodes (GDE) were investigated during the half-cell measurements. They consist of a gas diffusion layer (GDL) with a microporous layer (MPL, Freudenberg H23 C2) and a catalyst layer (CL) on top. The CL was spray-coated with an airbrush system. The ink was prepared with the Pt/C or Ag/C catalyst, a 60 wt% PTFE dispersion in water (Sigma-Aldrich), 4 ml water, and 4 ml isopropanol. Three different commercial platinum on carbon catalysts were studied with a Pt ratio of 20% (HiSPEC®3000, Thermo Scientific), 40% (HiSPEC®4000, Alfa Aesar), and 60% (HiSPEC®9100, Thermo Scientific). Two synthesized Ag/C catalysts with 22% and 68% Ag content were also investigated. Before spraying, the ink was homogenized with a tip sonicator for 30 seconds. The spray-coating was performed on a heating plate at 80 °C to remove all volatile substances. Between the spraying of each layer, the ink was placed in an ultrasonic bath to preserve the homogenous distribution. Electrodes with a metal loading of 0.3 mg cm^{-2} and 8–13% PTFE in the dry CL were prepared.

The electrochemical measurements of the GDEs were performed with a Zennium potentiostat (Zahner Elektrik) in a commercially available half-cell (FlexCell® PTFE, Gaskatel). The active surface area of the GDE amounts to 3 cm^2, defined by the silicone gasket. An RHE Mini-HydroFlex (Gaskatel) served as RE, and a platinum-iridium wire as CE. During operation, the setup was heated to 50 °C via PTC heating elements integrated into the cell, and the temperature was monitored by a temperature control box (Gaskatel). The elevated temperature and the 4 M KOH electrolyte mimic the actual conditions of applications like alkaline fuel cells or metal-air batteries. The measurements with the GDE half-cell were carried out according to a protocol inspired by previous works with this half-cell in acidic media.[16,18,22] Table S3 details the procedure for the electrochemical measurements with the GDE half-cell. Before starting the measurement under nitrogen or oxygen flow, the gas was purged for at least 45 minutes to ensure the respective gas's saturation. A post-correction was performed for all electrochemical measurements with the GDE half-cell shown in this work using the uncompensated resistance (iR drop). The iR drop was determined with EIS by taking the measured real part resistance at the high-frequency intercept with the x-axis from the Nyquist plot.

In addition, a series of EIS were recorded at different current densities. The exact values can be taken from Table S3. Clear outliers were removed from the data to provide high-quality data for further processing. EIS data are commonly fitted with a proper equivalent circuit. However, this requires some prior knowledge about the investigated system. The Distribution of Relaxation Times (DRT) analysis offers an alternative way. Here, the impedance data are fitted with a series of RC elements, and each RC element produces a peak in the DRT plot, which is related to a specific physicochemical process.[36,37] DRT analyses were already reported for the HT-PEMFC,[38–40] the electrochemical hydrogen pump,[41] and the vanadium redox flow battery.[42,43] This work's DRT analysis was conducted with the ec-idea software, which is also applicable to inductive contributions.[44] A regularization parameter of 0.5 was selected. The parameter was reduced until the reconstructed impedance spectrum from DRT best fits the measured impedance spectrum. An even lower value would not improve the fit of the two spectra but would introduce some artificial peaks in the DRT plot due to measurement uncertainty.[41]

The electrochemical active surface area (ECSA) of Pt was calculated using Equation (4). Q_H represents the charge of hydrogen underpotential deposition, [*Pt*] the platinum loading in the electrode, and 0.21 mC cm^{-2} the specific charge for a monolayer of hydrogen on Pt.

$$ECSA = \frac{Q_H}{0.21\ [Pt]} \quad (4)$$

2. Results and Discussion

2.1. Characterization of the Catalyst

Figures 1a, b, and c show scanning electron microscope (SEM) images of the 20%, 40%, and 60% Pt/C catalysts. The platinum nanoparticles are barely visible as bright small dots with just a few nanometers and are located on the significantly larger carbon particles. The 40% Pt/C appears to have more nanoparticles than the 20% Pt/C, which is expected due to its higher platinum-to-carbon ratio. However, the 60% Pt/C does not follow the trend but exhibits agglomerations composed of individual platinum particles.

The 22% and 68% Ag/C catalysts have larger silver particles that tend to agglomerate, as presented in Figures 1d and e. Although it is difficult to distinguish the silver particles from the carbon, the small bright particles can be identified as silver. SEM images at lower magnification were also taken (Figures S3a, b). In the case of 68% Ag/C, large particles consisting of silver, several hundred nanometers in size, can be detected. However, in the case of 22% Ag/C, no such large particles can be seen, as all silver particles are less than 100 nm in size. A high silver-to-carbon ratio in the synthesis seems to lead to more substantial Ag particle agglomeration.

The X-ray diffraction (XRD) patterns of the three commercial Pt/C and the two synthesized Ag/C catalysts reveal a face-centered cubic structure of platinum and silver (Figures 2a, b).

© 2024 The Authors. ChemElectroChem published by Wiley-VCH GmbH

21960216, 0, Downloaded from https://chemistry-europe.onlinelibrary.wiley.com/doi/10.1002/celc.202400563 by Karlsruher Institut F., Wiley Online Library on [23/01/2025]. See the Terms and Conditions (https://onlinelibrary.wiley.com/terms-and-conditions) on Wiley Online Library for rules of use; OA articles are governed by the applicable Creative Commons License

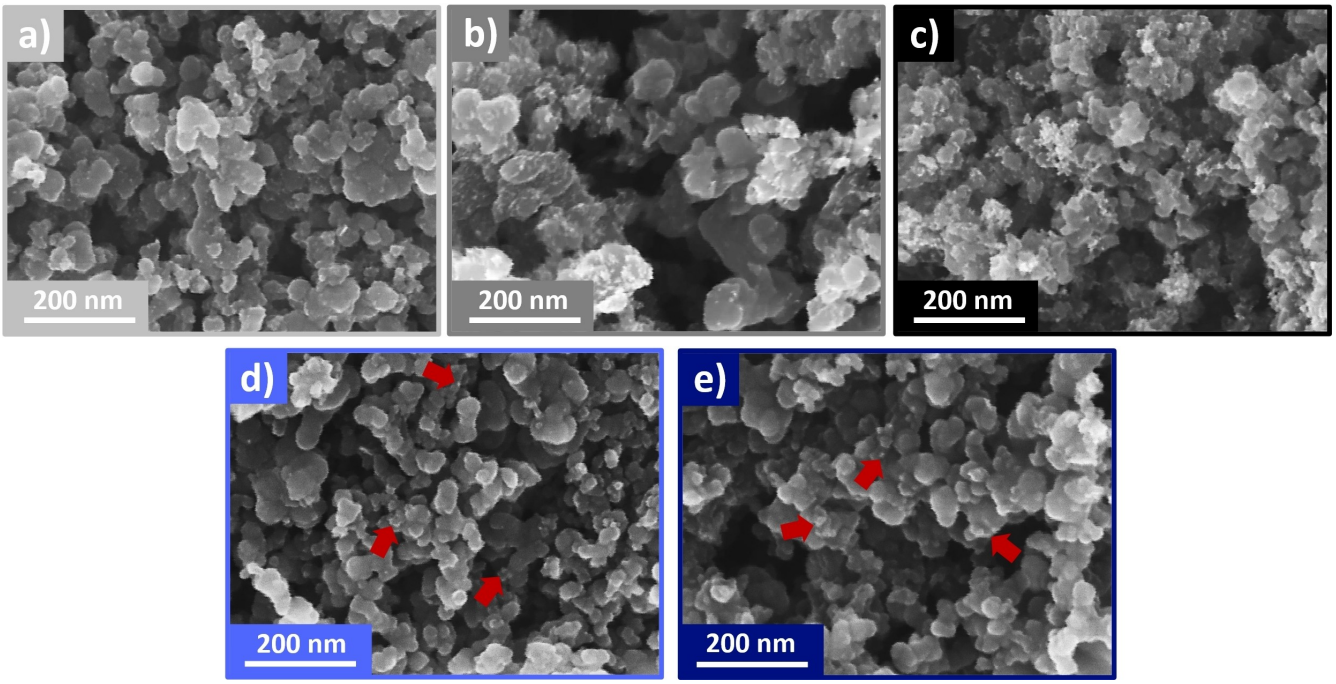

Figure 1. SEM images of a) 20% Pt/C, b) 40% Pt/C, c) 60% Pt/C, d) 22% Ag/C, and e) 68% Ag/C. The red arrows indicate exemplary silver particles.

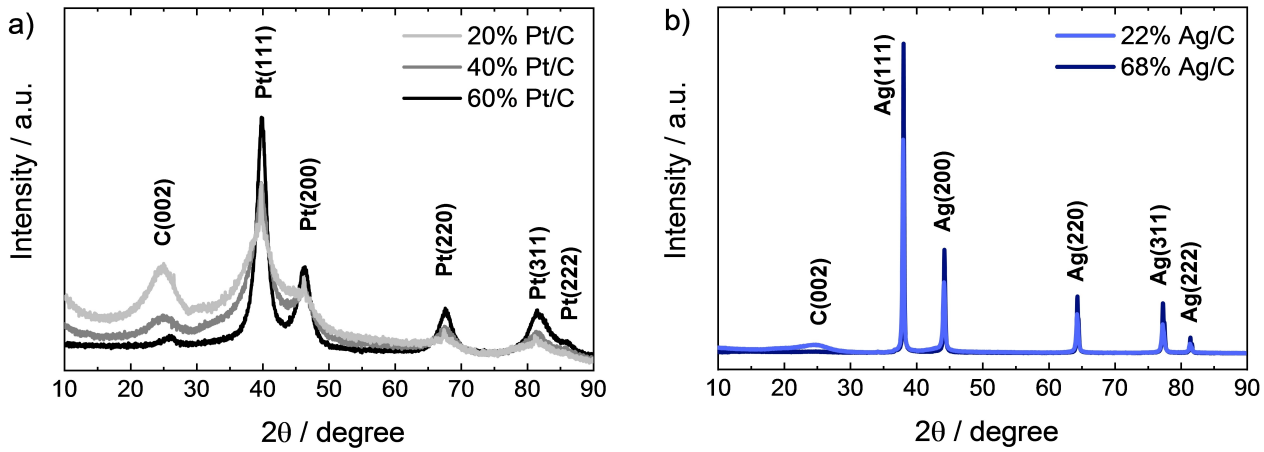

Figure 2. XRD patterns of a) Pt/C and b) Ag/C catalysts with different metal-to-carbon ratios.

Additionally, a broad reflection at around 25° can be detected, which can be assigned to graphite. The metal reflections become more prominent as the metal content in the sample increases, whereas the graphite reflection almost vanishes. No further reflections can be noticed, which testifies to a high purity of the catalysts. The mean crystallite size was determined via the Scherrer equation[45] with a shape factor *k* of 0.89 using the Pt(111) and the Ag(220) reflection. Mean crystallite sizes of 5.7 nm, 3.8 nm, and 5.0 nm were calculated for 20%, 40%, and 60% Pt/C, respectively. These values are in the same size range (2–10 nm) as other commercial Pt catalysts.[46] The mean crystallite sizes of Ag/C are larger with sizes of 25.1 nm and 31.9 nm for 22% and 68% Ag/C, respectively. This result explains the more defined reflections than that of Pt/C. The values are in a similar order of magnitude as the 15.0 nm obtained by Garcia et al. for the 10% Ag/C.[28] This indicates that the smaller the silver-to-carbon ratio, the smaller the crystallite size.

The silver-to-carbon ratio was determined by thermogravimetric analyses (TGA), as shown in Figure S4. The theoretical values for the Ag/C catalysts defined by the stoichiometry of the reactants were 20% and 60% Ag/C, but the corresponding values obtained from the TGA were 22% and 68%, respectively. In addition, the carbon support of the Ag/C catalyst decomposes at a significantly lower temperature compared to pure carbon black (CB), indicating that Ag catalyzes the combustion of CB. This observation has been described in previous publications.[47,48]

© 2024 The Authors. ChemElectroChem published by Wiley-VCH GmbH

21960216, 0, Downloaded from https://chemistry-europe.onlinelibrary.wiley.com/doi/10.1002/celc.202400563 by Karlsruher Institut F., Wiley Online Library on [23/01/2025]. See the Terms and Conditions (https://onlinelibrary.wiley.com/terms-and-conditions) on Wiley Online Library for rules of use; OA articles are governed by the applicable Creative Commons License

21960216, 0, Downloaded from https://chemistry-europe.onlinelibrary.wiley.com/doi/10.1002/celc.202400563 by Karlsruher Institut F., Wiley Online Library on [23/01/2025]. See the Terms and Conditions (https://onlinelibrary.wiley.com/terms-and-conditions) on Wiley Online Library for rules of use; OA articles are governed by the applicable Creative Commons License

2.2. RRDE Measurements

Figure S5a shows the cyclic voltammetry (CV) scans of a Pt disk electrode in an electrolyte with different KOH concentrations. All three CV scans correspond to the typical CV shape of a polycrystalline Pt electrode in an alkaline electrolyte.[49–51] The change in KOH concentration strongly affects the hydrogen underpotential deposition (H_{UPD}) peaks in the potential range of 0.2–0.4 V. The H_{UPD} oxidation peaks decrease and the peak corresponding to the (100) facet slightly shifts towards more negative potential with increasing KOH concentration. However, the H_{UPD} reduction peaks show no clear trend with increasing concentration. The changes in height and position of the H_{UPD} peaks indicate the sluggish hydrogen adsorption and desorption process on Pt. Similar observations were made by Wiberg et al. when changing the scan rate.[49]

The oxidation peak close to 0.85 V becomes more defined at higher concentrations, and the hydroxide adsorption on the Pt surface starts at more negative potentials. In addition, the total charge related to hydroxide adsorption and the oxidation of Pt increases. The higher amount of hydroxide in the solution increases the adsorption tendency. Even though the Pt reduction peak at 0.82 V is almost identical in height and position at different concentrations, the desorption of oxygenated species becomes more pronounced in the double-layer region at higher concentrations. This observation illustrates the increased irreversibility of Pt oxidation at higher concentrations.

The CV measurements on an Ag disk electrode shown in Figure S5b were performed at identical KOH concentrations as the Pt disk electrode. Only a few CVs of Ag in a nitrogen-saturated alkaline electrolyte are reported in the literature, which differ from each other and the ones shown here regarding the number and position of peaks.[8,32,52] Different crystal facets in the respective works might influence the electrochemistry. The peaks for Ag only correspond to the adsorption and desorption of hydroxide since the formation of Ag_2O would occur at potentials above 1.18 V.[32] All CVs of the Ag electrode display only a few features but a higher capacitive current compared to the Pt electrode. This observation is consistent with the CVs reported in the literature.[8,32,52] The capacitive current increases with higher KOH concentrations, especially when comparing 0.1 M KOH and 1.0 M KOH. This feature may be caused due to stronger adsorption of oxygenated species at higher KOH concentrations.

Furthermore, small peaks are visible at higher concentrations. The CV in 1.0 M KOH contains a broad oxidation peak at 0.40 V and two reduction peaks at 0.35 V and 0.50 V. All peaks shift towards slightly more positive potentials in 4.0 M KOH and increase in size. In addition, an oxidation peak appears at 0.60 V. The shift of the peaks and their overall shape could indicate a rather sluggish process of the hydroxide adsorption and desorption on Ag compared to the process on Pt. This result is consistent with the reported weaker affinity of oxygenated species towards Ag and the higher reversibility of the hydroxide adsorption on Ag compared to Pt.[32]

Figure 3a displays ORR polarization curves of Pt at a scan rate of 50 mV s^{-1} in 0.1 M KOH at various rotation rates. The current curves are almost identical for both scan directions and only display a hysteresis at around 0.8 V due to the adsorption and desorption of oxygenated species. In addition, the negative scan at a rotation rate of 100 rpm shows a peak at around 0.8 V, which can be assigned to the desorption of oxygen species as previously reported in the CV in nitrogen-saturated solution (see Figure S5a). The background correction could not entirely remove this peak. It seems that the Pt oxidation to PtO and its reduction is enhanced in an oxygen-saturated electrolyte. A spike can be observed close to 0.0 V, an artifact from the background subtraction. In this potential region, an accurate background correction is complex due to the onset of the hydrogen evolution reaction (HER).

Figure 3a additionally displays the corresponding ring current densities. They correlate with the share of formed peroxide and the number of transferred electrons shown in Figure 3b, which can be calculated via Equations (2) and (3). Almost no peroxide formation (ca. 1 %) is observed between 0.3 and 0.7 V, which implies almost exclusively a four-electron pathway for the ORR in this potential window. However, two potential regions can be identified where peroxide formation occurs: at around 0.8 V, close to the onset potential of the negative scan, and below 0.3 V in both scan directions. At around 0.8 V, the desorption of oxygenated species starts. In literature, it is widely described that the adsorbed oxygen species on the electrode surface block and inhibit the oxygen adsorption and favor the peroxide formation.[14,53,54]

Ramaswamy et al.[54,55] proposed a model to explain this behavior in detail. They predicted that if the Pt surface is not entirely covered with hydroxyl adsorbates, the oxygen could reach the surface and bind to it via chemisorption to undergo the four-electron pathway. In case of an increased coverage with hydroxyl species, the dissolved oxygen cannot reach the Pt surface anymore and is only loosely bound via a hydrogen bond to a hydroxyl species, which is adsorbed on the electrode. Due to less weakening of the oxygen bond, the oxygen will preferably react to peroxide instead of hydroxide. Similar observations were reported by Marković et al.[53] In addition, they observed an influence of the facets. The Pt(111) facet shows no peroxide formation in this region, unlike Pt(100) and Pt(110). They assume different types of hydroxide adsorption, reversible adsorption on Pt(111), and irreversible adsorption on the other facets.

Furthermore, it can be seen in Figure 3b that the peroxide formation at around 0.8 V is only visible in the negative scan due to the substantial coverage of the surface with oxygenated species when scanning from high potentials. In contrast, the surface is almost free from oxygen species when scanning from low potentials. Additionally, more peroxide is detected with increasing rotation rate since the formed peroxide is more easily detached from the electrode and will not undergo further reduction by the $2e^- + 2e^-$ pathway. In the mentioned potential region, the share of formed peroxide amounts up to 20 % when measuring at a scan rate of 50 mV s^{-1} and decreases to 10 % at 200 mV s^{-1}. The increased exposure time of the Pt surface to high potentials enhances Pt oxidation. Therefore, these observations indicate a correlation between the number of oxy-

© 2024 The Authors. ChemElectroChem published by Wiley-VCH GmbH

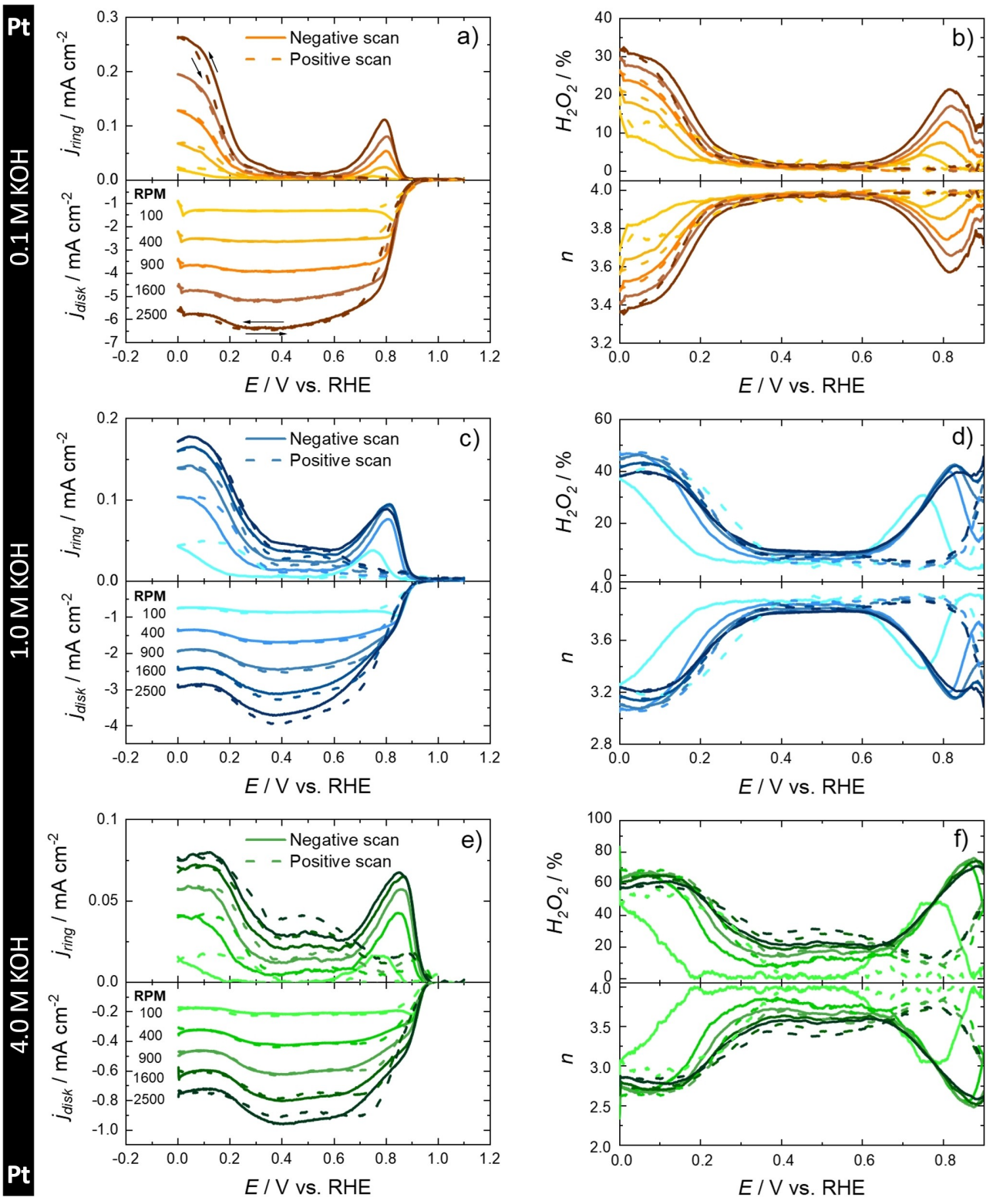

Figure 3. a), c), e) Ring and disk current densities, b), d), f) the share of formed peroxide, and the number of transferred electrons as a function of the disk potential with Pt as the WE. Scans were recorded at various rotation rates, and a scan rate of 50 mV s^{-1} in different KOH electrolytes, with RE = DHE and CE = carbon felt. The solid and the dashed line represent the negative and the positive scan, respectively.

genated species adsorbed on the Pt surface and the share of formed peroxide and thus seem to confirm the proposed mechanism from the literature[54] described previously.

However, on closer inspection, this model does not fully reflect the observations because the peroxide formation does not correlate with the amount of adsorbed oxygen species but

© 2024 The Authors. ChemElectroChem published by Wiley-VCH GmbH

21960216, 0, Downloaded from https://chemistry-europe.onlinelibrary.wiley.com/doi/10.1002/celc.202400563 by Karlsruher Institut F., Wiley Online Library on [23/01/2025]. See the Terms and Conditions (https://onlinelibrary.wiley.com/terms-and-conditions) on Wiley Online Library for rules of use; OA articles are governed by the applicable Creative Commons License

rather with its desorption (see Figures 3b and S5a). According to the model, peroxide formation is highest at the onset potential and significantly reduced when oxygenated species desorption occurs. Instead, the highest peroxide values are obtained at the desorption potential. Therefore, the pronounced peroxide formation in the potential region above 0.7 V mainly happens due to the desorption of oxygenated species, which act as bridging ligands between the platinum electrode and the solvated oxygen. During the sudden desorption of the bridging ligands, some oxygen reacts only incompletely to peroxide via the $2e^- + 2e^-$ pathway. The formed peroxide is then swept away from the disk electrode, producing a signal at the ring electrode.

The second potential region with peroxide formation starts at around 0.3 V, with the share of peroxide increasing towards the more negative potential limit of 0.0 V. Since hydrogen adsorption and desorption also happen in this potential region, research groups have proposed that the adsorbed hydrogen might block the oxygen adsorption, which will again favor the two-electron pathway.[30,53] Another explanation is based on the potential of zero total charge (PZTC) of Pt in aqueous electrolytes. The PZTC value of Pt is around 0.3 V, which causes the polarization of the electrode to change at this potential.[56] Thus, water molecules on the electrode surface will undergo a molecular rotation when the PZTC is passed, and their orientation will change from the oxygen end towards the electrode (the flip-up state of water) to an orientation with the hydrogen atoms towards the electrode (the flip-down state of water).[54,56,57] In the second case, the hydrogen atoms are no longer easily accessible, which changes the ORR reaction path.[54] Like the previous potential range, an increased peroxide formation can be observed at higher rotation rates (see Figure 3b).

RRDE measurements were also performed at higher KOH concentrations to understand the underlying mechanism of the ORR reaction. Furthermore, these measurements are close to technical cell conditions, using electrolytes with high alkaline concentrations.

Figures 3c and e show ORR polarization curves at 50 $mV s^{-1}$ in 1.0 M and 4.0 M KOH, respectively. The current density is strongly reduced due to significantly lower oxygen solubility at higher KOH concentrations.[58] Furthermore, the curves are more bent in the mixed controlled potential region than in 0.1 M KOH. The curves in the negative scan direction initially indicate a sharp drop coming from high potential, and at around 0.83 V and 0.90 V in 1.0 M and 4.0 M KOH, respectively, a kink appears. At these potentials, the peroxide formation is at its maximum (see Figures 3d and f). Compared to 0.1 M KOH, the peroxide formation in this potential range is doubled in 1.0 M KOH and more than tripled in 4.0 M KOH. It reaches a share of up to 40% and 70%, respectively. No apparent kink is visible in the positive scan of the polarization curve. Instead, the curve has a lower gradient mainly caused by the increased hydroxide adsorption on the electrode surface, blocking active sites and thus reducing the current density at potentials close to the onset potential. In the positive scan, no increased peroxide formation is visible. This observation confirms the previous assumption that hydroxyl adsorbates are not the main reason for the strong peroxide formation in this potential window but the desorption of oxygenated species. Additionally, the increased peroxide formation at higher concentrations can be explained by the increased adsorption tendency of hydroxide, resulting in a stronger desorption, which promotes peroxide formation.

Furthermore, the almost peroxide-free potential range between 0.3 and 0.7 V in 0.1 M KOH (see Figure 3b) is decreased to 0.3–0.6 V in 1.0 M and 4.0 M KOH (see Figures 3d and f). It correlates with the broadening of the Pt reduction peak in Figure S5a at higher KOH concentrations. In the mid-potential region, a peroxide share of 5–10% and 10–30% is reached depending on the rotation rate in 1.0 M and 4.0 M KOH, respectively. This peroxide formation can be attributed to irreversibly adsorbed oxygenated species on the electrode surface, which leads to a change in the reaction pathway toward the $2e^- + 2e^-$ mechanism. Since more oxygen species are irreversibly adsorbed in higher KOH concentrations on the electrode surface, an increased peroxide share is reached.

Compared to 0.1 M KOH, the peroxide formation at potentials below 0.3 V increases by approximately the same value as that in the mid-potential range (0.3–0.6 V). This means that irreversibly adsorbed oxygen species are responsible for increasing peroxide formation at higher KOH concentrations at potentials below 0.6 V.

Figure 4a displays the ORR polarization curves for an Ag disk electrode at 50 $mV s^{-1}$ at various rotation rates. The limiting current densities are similar to the Pt disk, indicating a four-electron pathway. However, contrary to Pt, the current decreases around 0.2 V. This effect is pronounced at higher rotation rates. In addition, a peak of the ring current density (see Figure 4a) and the highest share of peroxide formation of up to 33% (see Figure 4b) is observed at this potential. The CV in a nitrogen-saturated electrolyte displays no clear peak in this region due to a very high capacitive current (see Figure S5b). Literature data for different Ag catalysts show peroxide shares between 1% and 20% over a similar potential range.[32,59] Interestingly, increased peroxide formation can only be observed in the potential range, where hydroxide adsorption and desorption for the Ag electrode typically occur, and not at more positive potentials, where hydroxyl adsorbates should still be adsorbed on the electrode surface. Therefore, the mechanism for peroxide formation does not depend directly on the coverage of the electrode with hydroxyl species but rather on the actual adsorption/desorption process, as previously described for Pt as well. Unlike Pt, an increased peroxide formation is also visible in the positive scan direction due to Pt and Ag's different adsorption and desorption behavior. In the case of Pt, the adsorption/desorption of oxygenated species is irreversible, which can be recognized by the distance between the corresponding peaks (see Figure S5a). In contrast, hydroxide's adsorption/desorption process on Ag is known to be reversible and thus occurs at the same potential value.[32] Therefore, the increased peroxide formation in the positive scan in Figure 4b could be explained by the high reversibility of the adsorption/desorption of hydroxide on Ag since the adsorption of

© 2024 The Authors. ChemElectroChem published by Wiley-VCH GmbH

21960216, 0, Downloaded from https://chemistry-europe.onlinelibrary.wiley.com/doi/10.1002/celc.202400563 by Karlsruher Institut F., Wiley Online Library on [23/01/2025]. See the Terms and Conditions (https://onlinelibrary.wiley.com/terms-and-conditions) on Wiley Online Library for rules of use; OA articles are governed by the applicable Creative Commons License

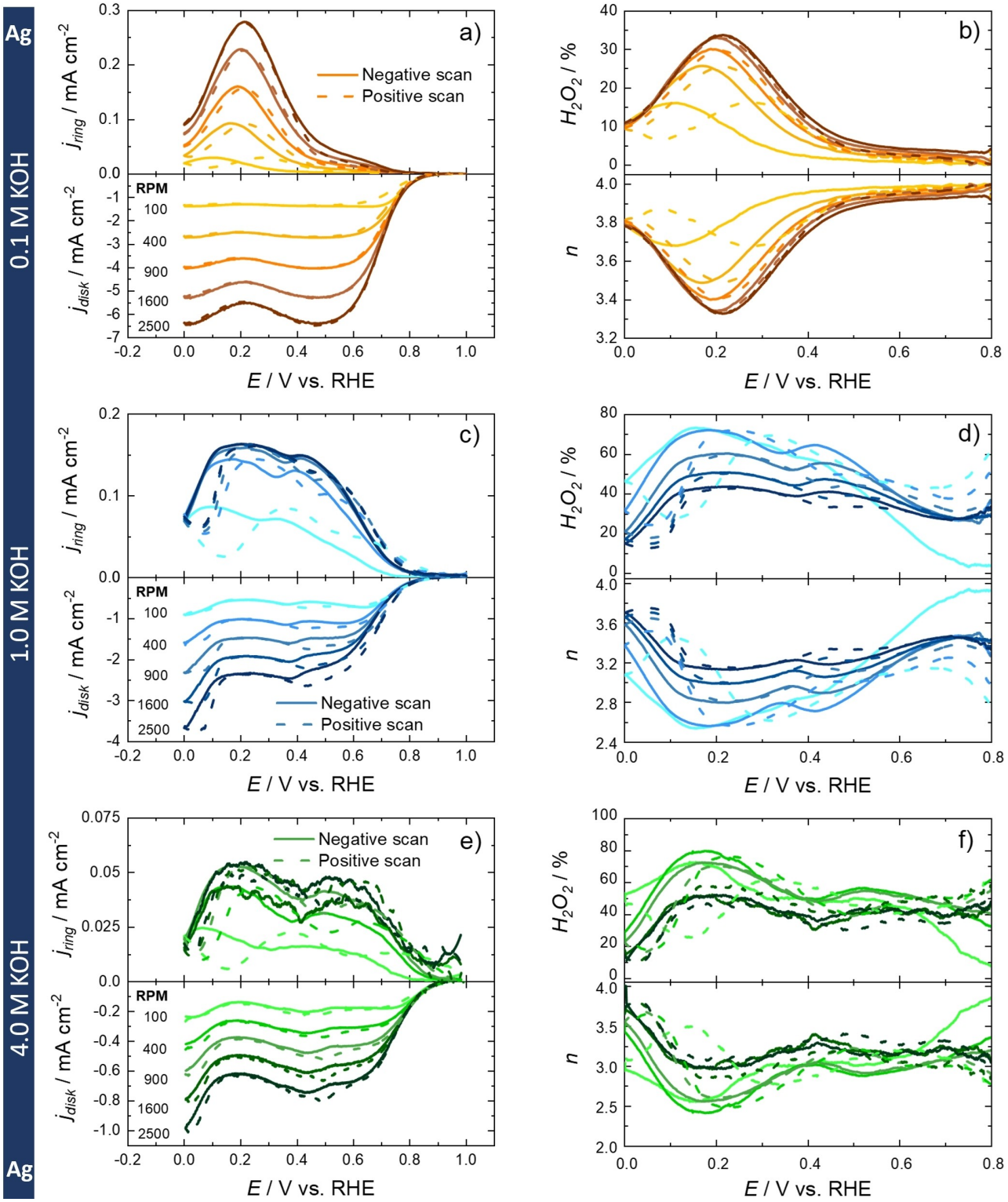

Figure 4. a), c), e) Ring and disk current densities, b), d), f) the share of formed peroxide, and the number of transferred electrons as a function of the disk potential with Ag as the WE. Scans were recorded at various rotation rates, and a scan rate of 50 mV s^{-1} in different KOH electrolytes, with RE = DHE and CE = carbon felt. The solid and the dashed line represent the negative and the positive scan, respectively.

hydroxides in the positive scan coincides with its desorption due to the dynamic equilibrium at that potential region.

Looking at the ring current density and the related share of formed peroxide in Figures 4a and b, a shift of the curves for the different scan directions can be observed. This effect is especially pronounced for lower rotation and higher scan rates, at which the ring current peak is shifted to lower potentials in the negative scan and higher potentials in the positive scan.

© 2024 The Authors. ChemElectroChem published by Wiley-VCH GmbH

21960216, 0, Downloaded from https://chemistry-europe.onlinelibrary.wiley.com/doi/10.1002/celc.202400563 by Karlsruher Institut F., Wiley Online Library on [23/01/2025]. See the Terms and Conditions (https://onlinelibrary.wiley.com/terms-and-conditions) on Wiley Online Library for rules of use; OA articles are governed by the applicable Creative Commons License

The system has more time to reach the equilibrium state at lower scan rates and can reach the equilibrium faster at higher rotation rates. Accordingly, the adsorption/desorption processes and the peroxide formation are delayed at higher scan rates and slower rotation rates. In addition, the share of peroxide formation increases at higher rotation rates. As for Pt, this can be attributed to the easier detachment of the formed peroxide from the electrode surface at higher rotation rates, prohibiting a subsequent reduction of the peroxide to the hydroxide product. This behavior indicates that a sequential $2e^- + 2e^-$ pathway and a direct-four electron pathway could occur simultaneously.

Figures 4c and e show the ORR polarization curves for the Ag disk electrode in 1.0 M and 4.0 M KOH solution. At higher KOH concentrations, the limiting current between 0.2 and 0.6 V is less flat, and the current density strongly increases below 0.1 V. In the potential range of the limiting current (0.2–0.6 V), an enhanced share of peroxide formation of 40% to 80% can be observed (see Figures 4d and f), which strongly reduces to around 10% to 50% at 0.0 V. Similar results were shown by Adanuvor et al.[60] in 6.5 M NaOH. They measured down to −0.2 V and could detect two limiting currents, one closer to the two-electron pathway and the other closer to the four-electron pathway. They concluded these observations best fit a sequential mechanism ($2e^- + 2e^-$ pathway). However, Kandaswamya et al.[8] have reported little peroxide formation over a wide potential range in 11 M NaOH when using "pure" salt and a significant increase of peroxide formation with "impure" NaOH. According to the manufacturer, the main impurity is sodium carbonate, which could be responsible for the changed pathway. Nevertheless, the ORR measurement with "impure" alkali salt probably represents the industrial conditions far better.

The literature states that the ORR mechanism of Ag in alkaline media is similar to that of Pt.[1,10] However, our measurements conclude that Ag shows an enhanced peroxide formation over a larger potential range and a reduced peroxide formation in the onset region compared to Pt, especially at a rotation rate of 100 rpm (compare Figures 3f and 4f). Concerning a possible industrial application, the onset region and a rotation rate of 100 rpm are the most relevant factors since a technical electrode operates close to the onset potential to enable high voltages and does not experience any motion.

2.3. GDE Half-Cell Measurements

A GDE half-cell was used to study the ORR under technical conditions. The temperature was set to 50 °C, and 4 M KOH was used as an electrolyte, which is the condition identified by Xu et al.[61] under which an aluminum–air battery performs best.

Figure 5a displays polarization curves for various Pt/C and Ag/C catalysts. 60% Pt/C exhibits the best ORR performance. Nevertheless, all Pt catalysts have a similar onset potential of approximately 1.05 V, as shown in the logarithmic form of the polarization curve (Figure 5b). The Pt/C curves at currents below 10 mA cm^{-2} are similar, but catalysts with higher platinum ratios perform better at higher current densities. The 60% Pt/C catalyst follows the typical exponential function even at higher current densities. In contrast, the 20% and the 40% Pt/C show strong polarization losses below around 0.82 V. At that potential, a change in the gradient can be seen in the logarithmic representation of the polarization curve for the two Pt/C catalysts, indicating a shift in the reaction pathway. The reasons for this phenomenon will be discussed in detail later.

Above about 0.82 V, all Pt curves demonstrate the typical shape of a polarization curve, and the trend of the ORR activity is as follows: 20% < 40% < 60% Pt/C. This ORR activity trend was observed for the identical Pt catalysts in the HT-PEMFC and explained by facilitated mass transport of oxygen due to the thinner catalyst layer for the 60% Pt/C. However, the polarization curves in their studies have a regular shape.[62] Interestingly, the ECSAs determined from the CVs measured in oxygen-free media (refer to Figure S6a) are highest for 20% Pt/C with 38 m^2 g^{-1} compared to 24 and 21 m^2 g^{-1} for 40% and 60% Pt/C, respectively. This trend does not correlate with the crystallite

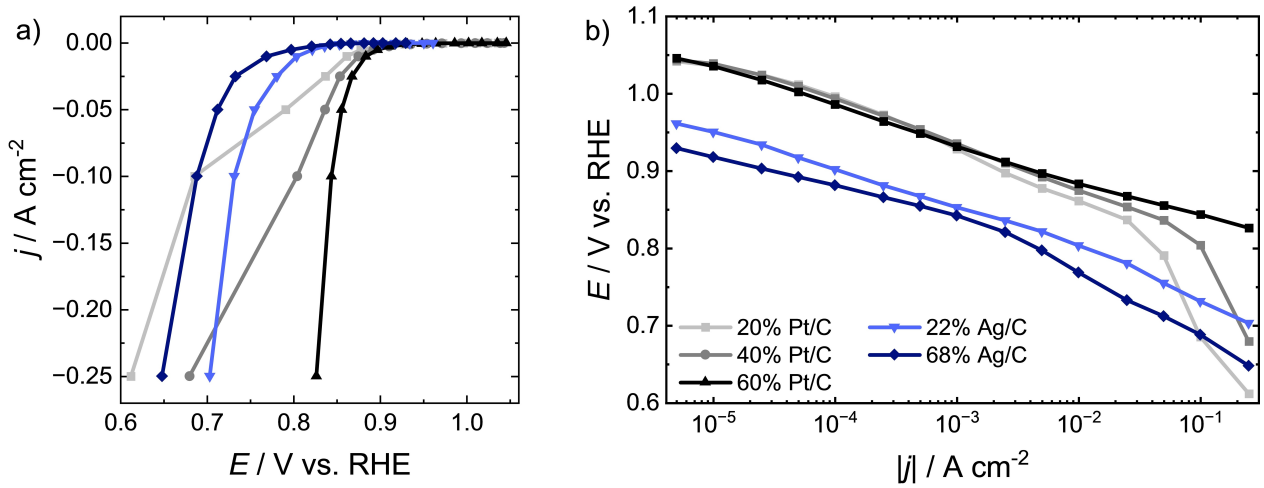

Figure 5. a) Polarization curves of different catalysts implemented into a GDE with a metal loading of 0.3 mg cm^{-2} and b) corresponding logarithmic representation of the polarization curves. Measurements were performed in the GDE half-cell at 50 °C in 4.0 M KOH.

© 2024 The Authors. ChemElectroChem published by Wiley-VCH GmbH

21960216, 0, Downloaded from https://chemistry-europe.onlinelibrary.wiley.com/doi/10.1002/celc.202400563 by Karlsruher Institut F., Wiley Online Library on [23/01/2025]. See the Terms and Conditions (https://onlinelibrary.wiley.com/terms-and-conditions) on Wiley Online Library for rules of use; OA articles are governed by the applicable Creative Commons License

size noted previously. The discrepancy may be explained by particles formed from several crystallites or particle agglomerations. Such agglomerations can be seen in the SEM image of 60% Pt/C (Figure 1c), resulting in a reduced ECSA compared to 20% Pt/C. Furthermore, there is no clear trend between the activity and the crystallite size. Nevertheless, the highest activity observed for the 60% Pt/C might be attributed to the facilitated oxygen transport due to the thinner catalyst layer and differences in the particle size distribution.

The silver catalysts show a lower activity than the platinum catalysts. The onset potential for the 22% and 68% Ag/C is 0.96 V and 0.93 V, respectively (Figure 5b). The 22% Ag/C catalyst demonstrates better ORR catalytic activity than the 68% Ag/C throughout the measured current regime. SEM and XRD results (Figure S3 and Figure 2b) indicate a lower mean crystallite and particle size for the 22% Ag/C catalyst. Reducing particle size is beneficial because it increases the ratio of surface to bulk atoms, resulting in a higher electrochemically active surface area. Contrary to the Pt/C, the thicker electrode performs better since the effect of the particle size may outperform the effect of the electrode thickness. Linge et al.[63] studied the effect of particle size on Ag nanowires with different diameters. They observed that a smaller Ag nanowire diameter leads to increased ORR performance.

The polarization curves of both Ag/C catalysts exhibit the typical exponential function, similar to 60% Pt/C (Figure 5a). Furthermore, the logarithmic depiction reveals a nearly straight slope for both catalysts (Figure 5b). This results in a more positive potential for 22% Ag/C than 20% and 40% Pt/C at $-250\ mA\,cm^{-2}$. 68% Ag/C has a more positive potential than 20% Pt/C at this current density. To our knowledge, this observation is the first time that a superior ORR performance of Ag compared to Pt has been reported under comparable and technical conditions. So far, this has only been demonstrated with an RDE setup for synthesized nanoporous Ag[64] and for Ag/Pt alloys.[65]

We will analyze the two extremes, 20% and 60% Pt/C, in more detail to better understand the reasons for the strong polarization losses observed for the 20% and 40% Pt/C shown in Figure 5.

Figures 6a and b show the 20% and 60% Pt/C polarization curves. Both curves are nearly identical in the activation polarization region at currents below $10\ mA\,cm^{-2}$. However, at larger current densities, the polarization curve for the 60% Pt/C catalyst still follows an exponential function, while a kink is observed for the 20% Pt/C catalyst. Such behavior was not detected in any publications for Pt catalysts studied in GDE half-cells in acidic electrolytes.[16–18,22] Furthermore, it cannot be explained by the mass transport limitation usually observed at high current densities since the applied current densities are moderate with a strong excess of oxygen supply. Moreover, the slope increases again at the last measurement point, indicating a higher gradient if the current is further increased.

Electrochemical impedance spectroscopy (EIS) measurements were performed at different current densities to gain deeper insights (Figures 6c, d). Specific measurement points on the polarization curve are highlighted, as they are recorded at the same current density as the corresponding EIS measurements. In Figure 6d, the semicircles observed in the Nyquist plot for the 60% Pt/C continuously decrease in size as the current density increases. The increased overpotential explains the decrease of the ORR charge transfer resistance on Pt at higher current densities, which was previously observed in proton exchange membrane fuel cells (PEMFC).[38,66] This trend reverses at high current densities because mass transport resistivity dominates. Since mass transport limitations are not reached under these operating conditions, the trend for 60% Pt/C fits perfectly with reports from the literature.[38,66]

A different behavior is observed for the impedance measurements with 20% Pt/C (Figure 6c). From the first to the second measured current density, the semicircle decreases, the third impedance spectrum slightly increases, and the fourth exhibits the largest semicircle. The impedance decreases when the current density is further increased, just like it was observed for 60% Pt/C. The Nyquist plot displays the same behavior as the polarization curve and thus confirms it. Additionally, inductive loops at low frequencies are present in the impedance measurements of the two highest current densities. This pseudo-inductive behavior has already been reported for fuel cells and originates mainly from the ORR.[67] Such a behavior can be explained by the slow removal of a site-blocking species, which leads to the unblocking of active metal sites. This reduces the charge transfer resistance of the ORR, particularly pronounced at low frequencies.[68,69] The impedance measurements at -30 and $-50\ mA\,cm^{-2}$ also indicate some instabilities in the low-frequency region.

These observations fit well with the results from the RRDE. The RRDE data show increased peroxide formation at around 0.8 V in the negative scan (Figure 3b), which coincides with the desorption of oxygenated species (Figure S5a). At a similar potential, the potential drops sharply in the polarization curve, and the resistance increases in the EIS data for the 20% Pt/C catalyst. Therefore, these trends can be linked to increased peroxide formation in that potential region due to the desorption of oxygenated species. Additionally, the inductive loops in the impedance measurements in Figure 6c at current densities of -100 and $-150\ mA\,cm^{-2}$ indicate that oxygen species' desorption takes place. The instabilities at low frequencies observed in the Nyquist plots at -30 and $-50\ mA\,cm^{-2}$ could be attributed to dynamic adsorption and desorption of oxygenated species.

The potential curve of the 60% Pt/C does not show a kink since the potential at which desorption of oxygenated species and simultaneously increased peroxide formation start is not reached in the examined current range. This is confirmed by the absence of inductive loops at low frequencies. This observation again emphasizes that it is not the adsorbed oxygenated species itself but rather the dynamic adsorption/desorption process of oxygenated species, especially hydroxides, responsible for the increased peroxide formation and thus leads to an increased polarization loss in this specific potential region. Besides the change in reaction mechanism to the two-electron pathway, the desorption of oxygenated species results

© 2024 The Authors. ChemElectroChem published by Wiley-VCH GmbH

21960216, 0, Downloaded from https://chemistry-europe.onlinelibrary.wiley.com/doi/10.1002/celc.202400563 by Karlsruher Institut F., Wiley Online Library on [23/01/2025]. See the Terms and Conditions (https://onlinelibrary.wiley.com/terms-and-conditions) on Wiley Online Library for rules of use; OA articles are governed by the applicable Creative Commons License

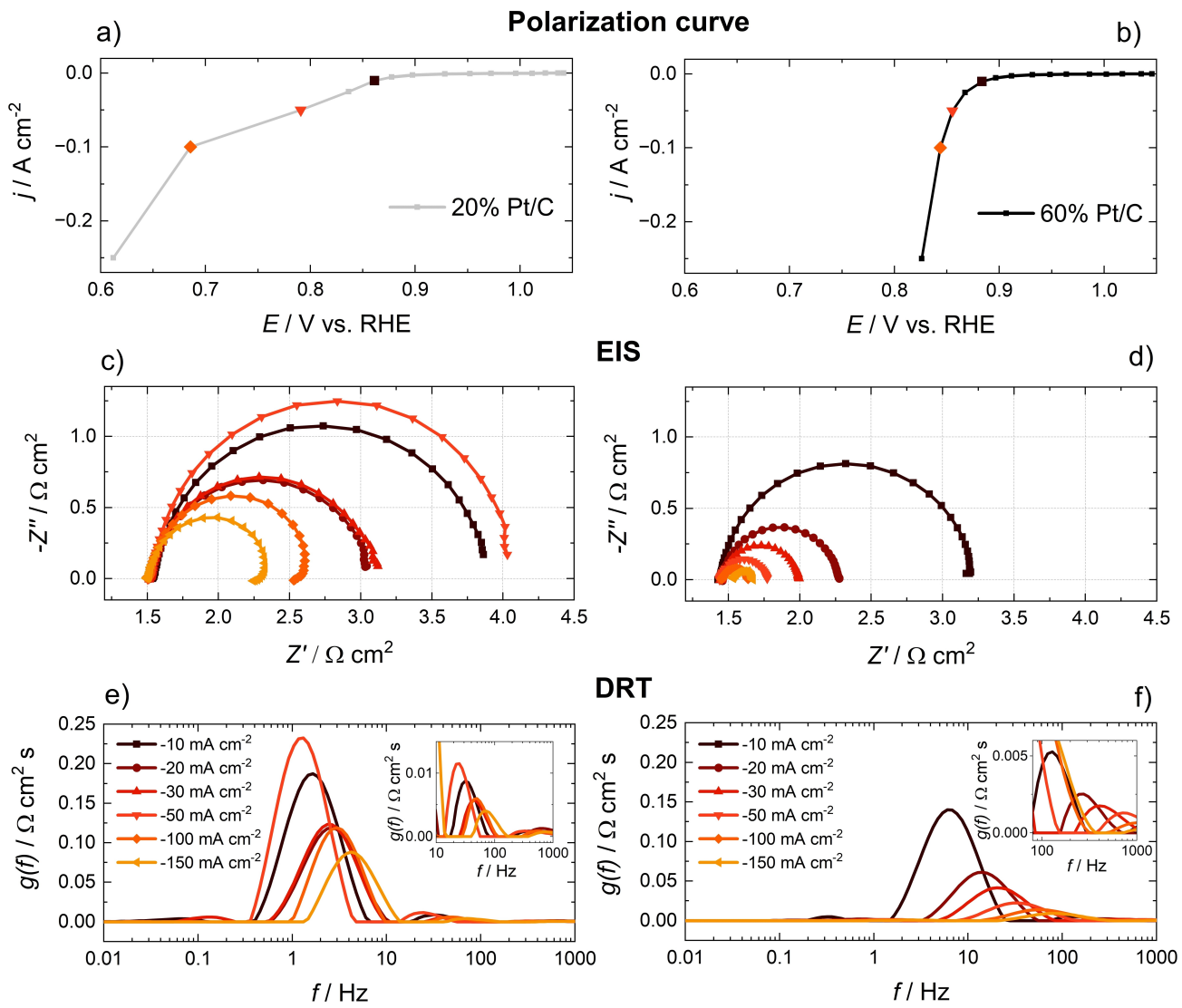

Figure 6. Comparison of 20% and 60% Pt/C catalysts implemented into a GDE with a platinum loading of 0.3 mg cm^{-2} in the GDE half-cell at 50 °C in 4.0 M KOH using: a), b) Polarization curves, c), d) Nyquist plots, and e), f) DRT analysis.

in an overall hindered ORR, leading to an activity decrease in this potential region.

It must also be considered that for the Pt/C catalysts in the GDE half-cell, the desorption occurs at around 0.59–0.89 V (Figure S6a), while for the Pt-RRDE it takes place at around 0.65–0.97 V (Figure S5a). The peroxide formation is most likely shifted by a similar potential. This result can explain the minor discrepancy in the potential for the appearance of increased peroxide formation at the RRDE and the anomalies at the GDE half-cell.

Furthermore, DRT analysis of the EIS measurements was performed (Figures 6e, f). The most prominent peak can be assigned to the ORR charge transfer resistance since it is the primary process. In addition, it is in a frequency range where the ORR was observed for the PEMFC.[38,66] A small peak at 0.1 Hz, which was unreliably detected, is likely caused by noise due to an unstable potential at low frequencies. A diffusion resistance was observed in air-operated PEMFCs between 1 and 10 Hz.[38,39,66] However, in the study by Weiß et al.[38] no mass transport-related peak could be identified when the high-temperature PEMFC (HT-PEMFC) was operated under pure oxygen at 300 mA cm^{-2}. The authors used the identical 20% Pt/C catalyst in their work. The absence of an increase in this peak at higher currents in this work suggests the absence of mass transport resistance in the current regime studied.

At higher frequencies, another peak is visible (see zoomed-in diagrams in Figures 6e, f), which shows the same trend as the prominent peak assigned to the ORR. Two ORR-related peaks have been identified for the HT-PEMFC,[38,39] while only one ORR peak is reported for the low-temperature PEMFC (LT-PEMFC).[66] Similar to the HT-PEMFC, the second peak could also be ORR-related and is probably linked to the interaction of an adsorbing anion during the ORR. In summary, the slope of the presented potential curves can only be attributed to the ORR kinetics itself, and the polarization loss observed at the 20% Pt/C is not mass transport driven.

© 2024 The Authors. ChemElectroChem published by Wiley-VCH GmbH

21960216, 0, Downloaded from https://chemistry-europe.onlinelibrary.wiley.com/doi/10.1002/celc.202400563 by Karlsruher Institut F., Wiley Online Library on [23/01/2025]. See the Terms and Conditions (https://onlinelibrary.wiley.com/terms-and-conditions) on Wiley Online Library for rules of use; OA articles are governed by the applicable Creative Commons License

Interestingly, the prominent peak is shifted by almost one order of magnitude from 1–4 Hz for 20% Pt/C to 6–80 Hz for 60% Pt/C, indicating that the 60% Pt/C catalyzes the ORR faster. The 60% Pt/C electrode is thinner than the 20% Pt/C since the platinum loading of 0.3 mg cm^{-2} is identical. Therefore, the shorter oxygen diffusion paths within the catalyst layer enable a quicker oxygen supply to the catalytically active sites, allowing a faster ORR. Additionally, the different carbon support of both catalysts may affect oxygen diffusion or electrolyte distribution in the GDE, thereby accelerating the ORR process.

Furthermore, the ORR peak for the 20% Pt/C follows the same trend as the corresponding impedance data and polarization curve. The impedance values for the studied current regime are 1.0–2.9 Ω cm^2 and 0.1–1.8 Ω cm^2 for 20% and 60% Pt/C, respectively. The ORR of 20% Pt/C is significantly inhibited at current densities of −30 and −50 mA cm^{-2}, exhibiting up to nine times higher impedances than 60% Pt/C. This current range corresponds to a potential region between 0.82 V–0.77 V, where an increased ORR charge transfer resistance is observed. The 60% Pt/C potential remains above 0.82 V in the investigated current range.

These results confirm the previous finding that the desorption of oxygenated species on Pt affects the slope of the polarization curve. The desorption causes a change in the reaction path toward the peroxide formation and inhibits the ORR at potentials below 0.82 V.

Additional measurements were conducted to investigate the behavior of 20% Pt/C. The reproducibility of the polarization curve was studied by repeating it five times in a row over four hours. The polarization curves are shown in Figure 7a, and the first five measurements (No. 1–5) exhibit high reproducibility over the entire examined current range. All five curves show a similar onset potential of approximately 1.05 V in the logarithmic representation and the previously discussed shape at higher current densities (Figure 7b). This result indicates mostly reversible adsorption and desorption of oxygenated species. At high potentials, particularly hydroxide, adsorption occurs while desorption occurs below 0.82 V, resulting in a weakened ORR.

In the second step, the setup was left to rest for 15 hours without applying any current. Afterward, three polarization curves (No. 6–8) were conducted. These curves show a decrease in ORR performance, as indicated by a shift toward more negative potentials (Figure 7a). Interestingly, the onset potential remains almost identical, and the curves in the logarithmic representation exhibit similar slopes with a gap to the previously measured curves (Figure 7b). Flooding as a cause can be excluded, as it would alter the polarization curve during several hours of galvanostatic cycling and significantly affect the onset potential. Instead, the electrode's exposure to open circuit potential in a highly concentrated alkaline electrolyte appears to have a much stronger effect than galvanostatic cycling. It is important to note that apart from a slight improvement in activity between the sixth and the following two curves at currents of around 10^{-5}–10^{-3} mA cm^{-2}, all three curves follow the same course. Irreversible oxidation occurs for 20% Pt/C at open circuit potentials in 4 M KOH. This oxidation is reversible only to a small extent, probably when hydroxyl adsorbates are eliminated by cycling towards more negative potentials, as in the sixth polarization curve.

In the final step, the setup was left for another 18 hours. The resulting polarization curve (Figure 7a, No. 9) shows a significant decrease in ORR activity. The curve has a typical shape, and in logarithmic form, it demonstrates a nearly straight slope with a barely recognizable kink at around 0.82 V (Figure 7b). The onset potential has decreased to 1.02 V, indicating a strong oxidation of Pt. The observation can be confirmed by examining CVs in oxygen-free media (Figure S7). The peak height exhibits continuous reduction from the initial CV over the CV after the first break until the last step. Similarly, the ECSA of Pt is reduced from initially 32 m^2 g^{-1} to 26 m^2 g^{-1} and then to 21 m^2 g^{-1}. Zhang et al.[70] have reported a similar reduction of ECSA after performing accelerated stress tests in perchloric acid by cycling in different potential regions. They determined Pt oxidation to be the main issue. However, Pt oxidation occurs through pure chemical oxidation without applying any current or potential in this work. Nevertheless, it still has a strong impact even in moderate time scales. This may be due to the

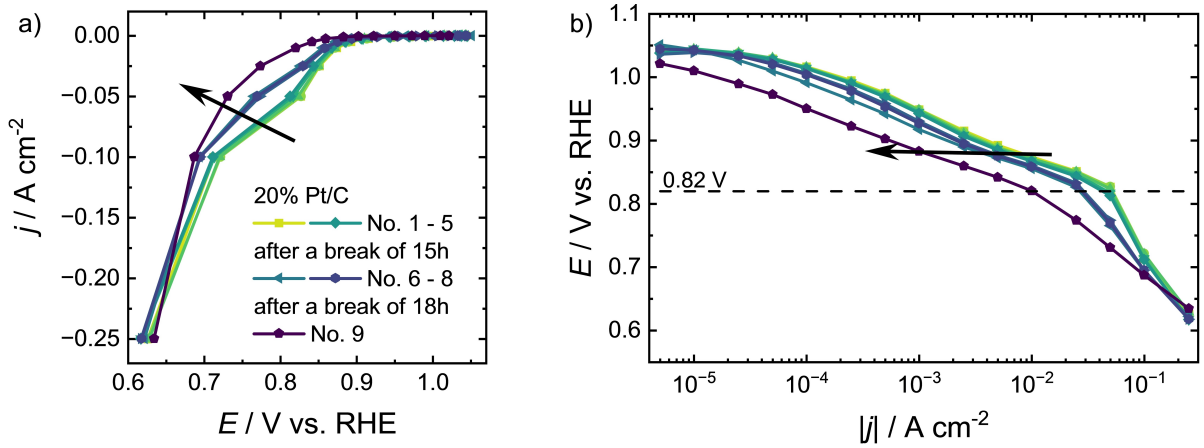

Figure 7. a) Polarization curves of 20% Pt/C implemented into a GDE with a metal loading of 0.3 mg cm^{-2} and b) logarithmic representation of the polarization curves. Measurements were performed in the GDE half-cell at 50 °C in 4.0 M KOH.

© 2024 The Authors. ChemElectroChem published by Wiley-VCH GmbH

21960216, 0, Downloaded from https://chemistry-europe.onlinelibrary.wiley.com/doi/10.1002/celc.202400563 by Karlsruher Institut F., Wiley Online Library on [23/01/2025]. See the Terms and Conditions (https://onlinelibrary.wiley.com/terms-and-conditions) on Wiley Online Library for rules of use; OA articles are governed by the applicable Creative Commons License

oxidative nature of the electrolyte. The strong irreversible oxidation can result from the so-called place-exchange conversion to PtO_2, which starts already at 0.6 V in the presence of oxygen.[71]

Furthermore, the polarization curves (Figure 7a) are impacted between 0.85 V and 0.7 V. The potential decay observed in this region was previously linked to the desorption of oxygenated species. However, this effect becomes less pronounced after resting as the Pt increasingly irreversibly oxidizes, reducing adsorbate desorption. Additionally, the change in slope in the logarithmic form (Figure 7b) becomes less apparent. However, the kink that indicates a change in slope is still slightly observable at around 0.82 V.

The impedance spectroscopy measurements support the observations at $-100\ mA\,cm^{-2}$. The Nyquist plot in Figure S8a shows a decrease in pseudo-inductive behavior over time, confirming the decrease in desorption of oxygenated species. The corresponding DRT plot reveals the absence of any significant mass transport resistance (Figure S8b). Flooding can, therefore, be excluded as a possible reason for the altered ORR performance. Instead, a decrease in ORR charge transfer resistance and an increase in frequency after each break can be observed. These results indicate that converting Pt metal to Pt oxide accelerates the ORR and reduces impedance. This is due to the decrease in the desorption of oxygenated species in this potential region, resulting in a reduced inhibition of the ORR. However, it is important to note that Pt oxidation also leads to decreased ORR activity.

Finally, the Pt/C and Ag/C catalysts are compared in detail by EIS measurements at $-100\ mA\,cm^{-2}$ (Figure 8a). The Nyquist plot reveals pseudo-inductive behavior for the 20% Pt/C and the 68% Ag/C, while the 40% Pt/C displays some instabilities at low frequencies. The 60% Pt/C and the 22% Ag/C do not show distinctive features at low frequencies. The pseudo-inductive behavior clearly indicates a slow desorption process of site-blocking species.[68,69] As previously mentioned, the instabilities observed at low frequencies may be due to a dynamic adsorption/desorption process. However, unlike 20% and 40% Pt/C, the 68% Ag/C exhibits a typical polarization curve shape (see Figure 5a). The higher reported reversibility of hydroxide adsorption on silver may explain this difference[32] and therefore reduced ORR inhibition during desorption. In addition, the RRDE detects significantly less peroxide formation on Ag than Pt near the onset potential at 100 rpm (compare Figures 3 and 4).

Furthermore, DRT analysis was performed, and the values corresponding to the ORR charge transfer are presented in Figure 8b. The prominent peak attributed to the ORR is almost exclusively visible, indicating that the impedance of every catalyst has only kinetic contributions in the examined current region. The ORR charge transfer resistance at $-100\ mA\,cm^{-2}$ is highest for 20% and 40% Pt/C with $1.37\ \Omega\,cm^{-2}$ and $1.16\ \Omega\,cm^{-2}$, respectively. This is closely followed by 68% Ag/C with $1.15\ \Omega\,cm^{-2}$. Compared to the other Pt/C catalysts, 60% Pt/C has the lowest charge transfer resistance of $0.18\ \Omega\,cm^{-2}$.

The dimension of the impedance values of the different Pt/C catalysts depends on whether the potential remains above 0.82 V. For 20% and 40% Pt/C, the corresponding potential values are 0.700 V and 0.780 V, respectively, while for 60% Pt/C it is 0.836 V. If the potential falls below 0.82 V desorption of oxygenated species starts, which inhibits the ORR and promotes peroxide formation.

Furthermore, the ORR charge transfer frequency obtained from the DRT analysis differs significantly for the different Pt/C catalysts (Figure 8b). The 20% and 40% Pt/C show a frequency of the ORR process below 6 Hz, while the 60% Pt/C exhibits one order of magnitude faster ORR kinetics at 54.9 Hz. The slower ORR process for the 20% and 40% Pt/C reflects the significant losses observed at the polarization curve in Figure 5a and supports again that the ORR is inhibited due to the desorption of oxygenated species. The catalyst layer thickness has little influence on the ORR kinetics, as the ORR frequencies of 20% and 40% Pt/C differ marginally. A value closer to 22% Ag/C would be expected without disturbances.

The Ag/C catalysts show an ORR frequency of 27.4 Hz and 69.2 Hz for 22% and 68% Ag/C, respectively, and are in the

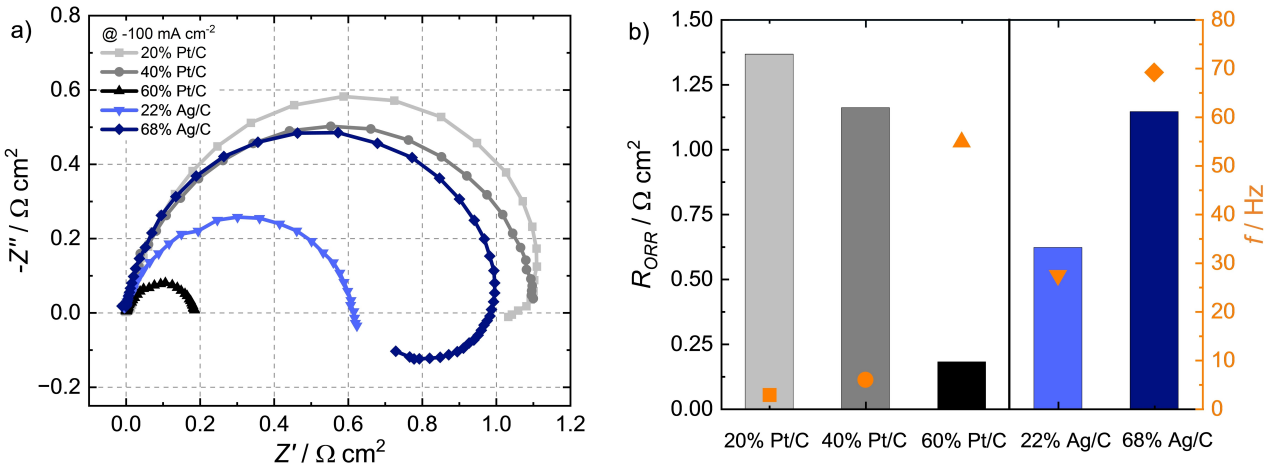

Figure 8. Comparison of Pt/C and Ag/C catalysts implemented into a GDE with a metal loading of $0.3\ mg\,cm^{-2}$ in the GDE half-cell at 50 °C in 4.0 M KOH using a) Nyquist plots and b) the ORR charge transfer resistance and the ORR characteristic frequency extracted from DRT analysis at $-100\ mA\,cm^{-2}$.

© 2024 The Authors. ChemElectroChem published by Wiley-VCH GmbH

21960216, 0, Downloaded from https://chemistry-europe.onlinelibrary.wiley.com/doi/10.1002/celc.202400563 by Karlsruher Institut F., Wiley Online Library on [23/01/2025]. See the Terms and Conditions (https://onlinelibrary.wiley.com/terms-and-conditions) on Wiley Online Library for rules of use; OA articles are governed by the applicable Creative Commons License

frequency range of 60% Pt/C (Figure 8b). The 68% Ag/C displays an almost twice as fast ORR process as the 22% Ag/C. The thinner catalyst layer enhances the supply of oxygen within the catalyst layer. However, the charge transfer resistance values reflect an opposite behavior. The values amount to 0.62 Ωcm^{-2} and 1.15 Ωcm^{-2} for the 22% and 68% Ag/C and can be explained by the smaller particle size in the 22% Ag/C case, which results in an increased number of active sites. This leads to improved ORR performance despite the slower ORR kinetic.

3. Conclusions

This work combines RRDE and GDE half-cell measurements to compare the ORR characteristics of Pt and Ag in alkaline media. The GDE half-cell results reveal substantial polarization losses below 0.82 V for the Pt catalysts, affecting the polarization curve's slope. In that potential range, DRT analysis detects an increase in charge transfer resistance and a decrease in the characteristic frequency of the ORR. In addition, the Nyquist plot reveals instabilities and an inductive loop at low frequencies, which is related to the desorption of adsorbed species. In the corresponding RRDE measurements, the polarization loss is correlated with an increased peroxide formation, which is especially pronounced in this potential range. Moreover, the peroxide formation and polarization slope change occur at potentials where oxygenated species desorb. The primary cause for increased peroxide formation and the associated polarization loss is more likely related to the desorption of hydroxyl adsorbates than the presence of adsorbed oxygenated species. This desorption alters the reaction mechanism towards the two-electron pathway and impedes the overall ORR process. A measurement of 20% Pt/C kept at open circuit potential for several hours reveals significant irreversible Pt oxidation. Due to the reduced desorption, a conversion towards a typical polarization curve occurs, although a loss of catalytic activity accompanies this process. In contrast, Ag does not show these polarization losses since the potential range where peroxide formation occurs is below the typical operating potential, particularly when considering a rotation rate of 100 rpm. Therefore, Ag/C catalyzes the ORR more effectively than some Pt/C catalysts at high current densities in high alkaline media. This was demonstrated under practical battery operating conditions.

A 60% > 40% > 20% Pt/C trend was determined for the catalytic activity in alkaline media. A thinner catalyst layer shows a beneficial behavior due to shorter oxygen pathways. In addition, different particle size distributions may affect the catalytic activity. On the other hand, a different catalytic behavior, 22% > 68% Ag/C, was observed for the Ag catalysts, where the smaller particle size outweighs the effect of the electrode thickness due to the larger electrochemically active area.

In this work, the DRT analysis was implemented as an analytical tool to separate different physicochemical processes. It determines the ORR charge transfer resistance and the characteristic frequency of the ORR. Under the experiment conditions, the reaction kinetic was the dominating contribution for the half-cell impedance. Furthermore, our study presents a general approach for evaluating ORR catalysts and investigating the reaction mechanisms under realistic operating conditions.

Author Contributions

Alexander Rampf: Conceptualization, Methodology, Formal analysis, Investigation, Data curation, Writing – original draft; Michael Braig: Formal analysis, Data curation, Writing – review & editing; Stefano Passerini: Project administration, Funding acquisition, Writing – review & editing; Roswitha Zeis: Conceptualization, Methodology, Supervision, Funding acquisition, Writing – review & editing.

Acknowledgements

This work is part of the ALU-STORE project (Aluminum Metal as Energy Carrier for Seasonal Energy Storage) funded by KIT Future Fields and contributes to the research performed at CELEST (Center for Electrochemical Energy Storage Ulm-Karlsruhe).

Conflict of Interests

The authors declare no conflict of interest.

Data Availability Statement

The data that support the findings of this study are available from the corresponding author upon reasonable request.

Keywords: Distribution of relaxation times (DRT) · GDE half-cell measurements · Oxygen reduction reaction (ORR) · Peroxide · Rotating ring-disk electrode (RRDE)

[1] X. Ge, A. Sumboja, D. Wuu, T. An, B. Li, F. W. T. Goh, T. S. A. Hor, Y. Zong, Z. Liu, *ACS Catal.* **2015**, *5*, 4643–4667.
[2] F. H. B. Lima, J. Zhang, M. H. Shao, K. Sasaki, M. B. Vukmirovic, E. A. Ticianelli, R. R. Adzic, *J. Phys. Chem. C* **2007**, *111*, 404–410.
[3] X. Wang, Z. Li, Y. Qu, T. Yuan, W. Wang, Y. Wu, Y. Li, *Chem* **2019**, *5*, 1486–1511.
[4] B. J. Glaister, G. M. Mudd, *Miner. Eng.* **2010**, *23*, 438–450.
[5] É. Lèbre, M. Stringer, K. Svobodova, J. R. Owen, D. Kemp, C. Côte, A. Arratia-Solar, R. K. Valenta, *Nat. Commun.* **2020**, *11*, 4823.
[6] A. Wieckowski, J. Spendelow, in *Encyclopedia of Applied Electrochemistry*, Springer, New York, NY, **2014**, pp. 1491–1496.
[7] H. Erikson, A. Sarapuu, K. Tammeveski, *ChemElectroChem* **2019**, *6*, 73–86.
[8] S. Kandaswamy, A. Sorrentino, S. Borate, L. A. Živković, M. Petkovska, T. Vidaković-Koch, *Electrochim. Acta* **2019**, *320*, 134517.
[9] M. Chatenet, L. Genies-Bultel, M. Aurousseau, R. Durand, F. Andolfatto, *J. Appl. Electrochem.* **2002**, *32*, 1131–1140.
[10] J. S. Spendelow, A. Wieckowski, *Phys. Chem. Chem. Phys.* **2007**, *9*, 2654–2675.

© 2024 The Authors. ChemElectroChem published by Wiley-VCH GmbH

21960216, 0, Downloaded from https://chemistry-europe.onlinelibrary.wiley.com/doi/10.1002/celc.202400563 by Karlsruher Institut F., Wiley Online Library on [23/01/2025]. See the Terms and Conditions (https://onlinelibrary.wiley.com/terms-and-conditions) on Wiley Online Library for rules of use; OA articles are governed by the applicable Creative Commons License

[11] Y. Li, Q. Li, H. Wang, L. Zhang, D. P. Wilkinson, J. Zhang, *Electrochem. Energy Rev.* **2019**, *2*, 518–538.
[12] N. Wang, S. Ma, P. Zuo, J. Duan, B. Hou, *Adv. Sci.* **2021**, *8*, 2100076.
[13] T. Miyazawa, T. Terachi, S. Uchida, T. Satoh, T. Tsukada, Y. Satoh, Y. Wada, H. Hosokawa, *J. Nucl. Sci. Technol.* **2006**, *43*, 884–895.
[14] W. Y. Yan, S. L. Zheng, W. Jin, Z. Peng, S. N. Wang, H. Du, Y. Zhang, *J. Electroanal. Chem.* **2015**, *741*, 100–108.
[15] S. S. Kocha, K. Shinozaki, J. W. Zack, D. J. Myers, N. N. Kariuki, T. Nowicki, V. Stamenkovic, Y. Kang, D. Li, D. Papageorgopoulos, *Electrocatalysis* **2017**, *8*, 366–374.
[16] K. Ehelebe, N. Schmitt, G. Sievers, A. W. Jensen, A. Hrnjić, P. Collantes Jiménez, P. Kaiser, M. Geuß, Y. P. Ku, P. Jovanovič, K. J. J. Mayrhofer, B. Etzold, N. Hodnik, M. Escudero-Escribano, M. Arenz, S. Cherevko, *ACS Energy Lett.* **2022**, *7*, 816–826.
[17] R. Loukrakpam, B. F. Gomes, T. Kottakkat, C. Roth, *J. Phys. Mater.* **2021**, *4*, 044004.
[18] N. Schmitt, M. Schmidt, G. Hübner, B. J. M. Etzold, *J. Power Sources* **2022**, *539*, 231530.
[19] J. Müller-Hülstede, T. Zierdt, H. Schmies, D. Schonvogel, Q. Meyer, C. Zhao, P. Wagner, M. Wark, *J. Power Sources* **2022**, *537*, 231529.
[20] N. Schmitt, M. Schmidt, J. E. Mueller, L. Schmidt, B. J. M. Etzold, *Electrochem. commun.* **2022**, *141*, 107362.
[21] M. Inaba, A. W. Jensen, G. W. Sievers, M. Escudero-Escribano, A. Zana, M. Arenz, *Energy Environ. Sci.* **2018**, *11*, 988–994.
[22] K. Ehelebe, D. Seeberger, M. T. Y. Paul, S. Thiele, K. J. J. Mayrhofer, S. Cherevko, *J. Electrochem. Soc.* **2019**, *166*, F1259–F1268.
[23] B. A. Pinaud, A. Bonakdarpour, L. Daniel, J. Sharman, D. P. Wilkinson, *J. Electrochem. Soc.* **2017**, *164*, F321–F327.
[24] N. Bogolowski, O. Ngaleu, M. Sakthivel, J. F. Drillet, *Carbon* **2017**, *119*, 511–518.
[25] D. Franzen, B. Ellendorff, M. C. Paulisch, A. Hilger, M. Osenberg, I. Manke, T. Turek, *J. Appl. Electrochem.* **2019**, *49*, 705–713.
[26] Y. Pei, D. P. Wilkinson, E. Gyenge, *Small* **2023**, *19*, 2204585.
[27] K. Ehelebe, T. Ashraf, S. Hager, D. Seeberger, S. Thiele, S. Cherevko, *Electrochem. commun.* **2020**, *116*, 106761.
[28] A. C. Garcia, L. H. S. Gasparotto, J. F. Gomes, G. Tremiliosi-Filho, *Electrocatalysis* **2012**, *3*, 147–152.
[29] R. Zhou, Y. Zheng, M. Jaroniec, S. Z. Qiao, *ACS Catal.* **2016**, *6*, 4720–4728.
[30] G. Zhang, Q. Wei, X. Yang, A. C. Tavares, S. Sun, *Appl. Catal., B* **2017**, *206*, 115–126.
[31] R. Jäger, E. Härk, P. E. Kasatkin, E. Lust, *J. Electrochem. Soc.* **2014**, *161*, F861–F867.
[32] B. B. Blizanac, P. N. Ross, N. M. Marković, *J. Phys. Chem. B* **2006**, *110*, 4735–4741.
[33] J. M. Linge, H. Erikson, M. Merisalu, V. Sammelselg, K. Tammeveski, *SN Appl. Sci.* **2021**, *3*, DOI 10.1007/s42452-021-04289-x.
[34] A. Savitzky, M. J. E. Golay, *Anal. Chem.* **1964**, *36*, 1627–1639.
[35] U. A. Paulus, T. J. Schmidt, H. A. Gasteiger, R. J. Behm, *Journal of Electroanalytical Chemistry* **2001**, *495*, 134–145.
[36] T. H. Wan, M. Saccoccio, C. Chen, F. Ciucci, *Electrochim. Acta* **2015**, *184*, 483–499.
[37] M. Schönleber, E. Ivers-Tiffée, *Electrochem. commun.* **2015**, *58*, 15–19.
[38] A. Weiß, S. Schindler, S. Galbiati, M. A. Danzer, R. Zeis, *Electrochim. Acta* **2017**, *230*, 391–398.
[39] N. Bevilacqua, M. A. Schmid, R. Zeis, *J. Power Sources* **2020**, *471*, 228469.
[40] N. Bevilacqua, T. Asset, M. A. Schmid, H. Markötter, I. Manke, P. Atanassov, R. Zeis, *J. Power Sources Adv.* **2021**, *7*, 100042.
[41] M. Braig, R. Zeis, *J. Power Sources* **2023**, *576*, 233203.
[42] M. Schilling, M. Braig, K. Köble, R. Zeis, *Electrochim. Acta* **2022**, *430*, 141058.
[43] K. Köble, M. Jaugstetter, M. Schilling, M. Braig, T. Diemant, K. Tschulik, R. Zeis, *J. Power Sources* **2023**, *569*, 233010.
[44] M. Hahn, S. Schindler, L. C. Triebs, M. A. Danzer, *Batteries* **2019**, *5*, 43.
[45] F. T. L. Muniz, M. A. R. Miranda, C. Morilla Dos Santos, J. M. Sasaki, *Acta Crystallogr., Sect. A: Found. Adv.* **2016**, *72*, 385–390.
[46] F. J. Nores-Pondal, I. M. J. Vilella, H. Troiani, M. Granada, S. R. de Miguel, O. A. Scelza, H. R. Corti, *Int. J. Hydrogen Energy* **2009**, *34*, 8193–8203.
[47] D. Gardini, J. M. Christensen, C. D. Damsgaard, A. D. Jensen, J. B. Wagner, *Appl. Catal., B* **2016**, *183*, 28–36.
[48] K. A. S. Fernando, V. G. Watson, X. Wang, N. D. McNamara, M. C. Jochum, D. W. Bair, B. A. Miller, C. E. Bunker, *Langmuir* **2014**, *30*, 11776–11784.
[49] G. K. H. Wiberg, M. Arenz, *J. Power Sources* **2012**, *217*, 262–267.
[50] M. Favaro, C. Valero-Vidal, J. Eichhorn, F. M. Toma, P. N. Ross, J. Yano, Z. Liu, E. J. Crumlin, *J. Mater. Chem. A* **2017**, *5*, 11634–11643.
[51] P. Rheinländer, S. Henning, J. Herranz, H. A. Gasteiger, *ECS Trans.* **2013**, *50*, 2163–2174.
[52] G. Orozco, M. A. C. Pérez, A. Rincón, C. Gutiérrez, *Langmuir* **1998**, *14*, 6297–6306.
[53] N. M. Markovic, H. A. Gasteiger, P. N. Ross, *J. Phys. Chem.* **1996**, *100*, 6715–6721.
[54] N. Ramaswamy, S. Mukerjee, *J. Phys. Chem. C* **2011**, *115*, 18015–18026.
[55] N. Ramaswamy, S. Mukerjee, *Adv. Phys. Chem.* **2012**, *491604*, 1–17.
[56] T. Iwasita, X. L. Xia, *J. Electroanal. Chem.* **1996**, *41*, 95–102.
[57] J. Bockris, M. A. Habib, *Electrochim. Acta* **1977**, *22*, 41–46.
[58] R. E. Davis, G. L. Horvath, C. W. Tobias, *Electrochim. Acta* **1967**, *12*, 287–297.
[59] Q. Wu, L. Jiang, L. Qi, L. Yuan, E. Wang, G. Sun, *Electrochim. Acta* **2014**, *123*, 167–175.
[60] P. K. Adanuvor, R. E. White, *J. Electrochem. Soc.* **1988**, *135*, 2509–2517.
[61] C. Xu, N. Herrmann, X. Liu, B. Horstmann, S. Passerini, *J. Power Sources* **2023**, *574*, 233172.
[62] T. Maiyalagan, S. Pasupathi, B. G. Pollet, *Electrocatalysis* **2015**, *6*, 155–162.
[63] J. M. Linge, D. Kozhemyakin, H. Erikson, S. Vlassov, N. Kongi, K. Tammeveski, *ChemCatChem* **2021**, *13*, 4364–4371.
[64] Y. Zhou, Q. Lu, Z. Zhuang, G. S. Hutchings, S. Kattel, Y. Yan, J. G. Chen, J. Q. Xiao, F. Jiao, *Adv. Energy Mater.* **2015**, *5*, 1500149.
[65] S. Yu, Q. Lou, K. Han, Z. Wang, H. Zhu, *Int. J. Hydrogen Energy* **2012**, *37*, 13365–13370.
[66] M. Heinzmann, A. Weber, E. Ivers-Tiffée, *J. Power Sources* **2018**, *402*, 24–33.
[67] A. Schiefer, M. Heinzmann, A. Weber, *Fuel Cells* **2020**, *20*, 499–506.
[68] S. Gottesfeld, *J. Electrochem. Soc.* **2022**, *169*, 124518.
[69] M. Ciureanu, H. Wang, *J. Electrochem. Soc.* **1999**, *146*, 4031–4040.
[70] Y. Zhang, S. Chen, Y. Wang, W. Ding, R. Wu, L. Li, X. Qi, Z. Wei, *J Power Sources* **2015**, *273*, 62–69.
[71] A. Kongkanand, J. M. Ziegelbauer, *J. Phys. Chem. C* **2012**, *116*, 3684–3693.

Manuscript received: October 3, 2024
Revised manuscript received: November 7, 2024
Version of record online: ■■, ■■

© 2024 The Authors. ChemElectroChem published by Wiley-VCH GmbH

21960216, 0, Downloaded from https://chemistry-europe.onlinelibrary.wiley.com/doi/10.1002/celc.202400563 by Karlsruher Institut F., Wiley Online Library on [23/01/2025]. See the Terms and Conditions (https://onlinelibrary.wiley.com/terms-and-conditions) on Wiley Online Library for rules of use; OA articles are governed by the applicable Creative Commons License

RESEARCH ARTICLE

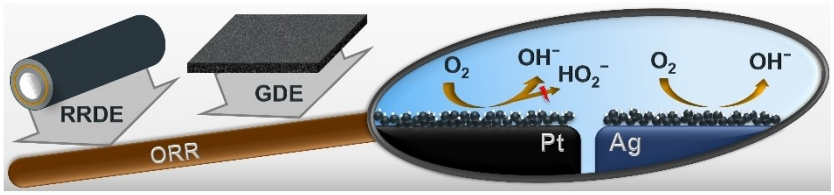

*A. Rampf, M. Braig, S. Passerini, R. Zeis**

In this study, the oxygen reduction reaction on Pt and Ag is investigated in alkaline media using fundamental and technical approaches. Strong differences at high currents are observed, leading to better performance for Ag under certain conditions. The underlying mechanistic electrocatalytic processes responsible for these phenomena are investigated and detected.

21960216, 0, Downloaded from https://chemistry-europe.onlinelibrary.wiley.com/doi/10.1002/celc.202400563 by Karlsruher Institut F., Wiley Online Library on [23/01/2025]. See the Terms and Conditions (https://onlinelibrary.wiley.com/terms-and-conditions) on Wiley Online Library for rules of use; OA articles are governed by the applicable Creative Commons License